Two Large-Scale Meteorological Patterns are Associated with Short-Duration Dry Spells in the Northeastern United States

RAYMOND SUKHDEO,[a] RICHARD GROTJAHN,[a] AND PAUL A. ULLRICH[a]

[a] *Department of Land, Air and Water Resources, University of California, Davis, Davis, California*

(Manuscript received 6 July 2023, in final form 25 September 2023, accepted 27 September 2023)

ABSTRACT: Large-scale meteorological pattern (LSMP)–based analysis is used in a novel way to understand meteorological conditions before and during short-duration dry spells over the northeastern United States. These LSMPs are useful to assess models and select better-performing models for future projections. Dry-spell events are identified from histograms of consecutive dry days below a daily precipitation threshold. Events lasting 12 days or longer, which correspond to ~10% of dry-spell events, are examined. The 500-hPa streamfunction anomaly fields for the first 12 days of each event are time averaged, and *k*-means clustering is applied to isolate the dry-spell-related LSMPs. The first cluster has a strong low pressure anomaly over the Atlantic Ocean, southeast of the region, and is more common in winter and spring. The second cluster has strong high pressure over east-central North America and is most common during autumn. Over the region, both clusters have negative specific humidity anomalies, negative integrated vapor transport from the north, and subsidence associated with a midlatitude jet stream dipole structure that reinforces upper-level convergence. Subsidence is supported by cold-air advection in the first cluster and the location on the east side of the lower-level high pressure in the second cluster. Extratropical cyclone storm tracks are generally shifted southward of the region during the dry spells. Individual events lie on a continuum between two distinct clusters. These clusters have similar local, but different remote, properties. Although dry spells occur with greater frequency during drought months, most dry spells occur during nondrought months.

SIGNIFICANCE STATEMENT: This study examines the large-scale weather patterns and meteorological conditions associated with dry-spell events lasting at least 2 weeks while affecting the northeastern United States. A statistical approach groups events together on the basis of similar atmospheric features. We find two distinct sets of patterns that we call large-scale meteorological patterns. These patterns reduce moisture, foster localized sinking, and shift the storm track southward along the Atlantic seaboard, all of which reduce precipitation. Besides greater understanding, knowing the meteorological patterns during short-term dryness in the region provides an important tool to assess how well atmospheric models reproduce these specific patterns. More dry spells occur in nondrought months than in drought months, which means that dry spells can occur without preexisting drought conditions.

KEYWORDS: North America; Ageostrophic circulations; Large-scale motions; Streamfunction; Drought; Extreme events

1. Introduction

The northeastern United States (hereinafter, the Northeast) (Fig. 1, red-outlined box) is densely populated with many economic interests, all of which rely on a heavily managed water supply. However, precipitation in this region has been changing (Melillo et al. 2014; Walsh et al. 2014). Despite a general wetting trend since the 1970s, climate change is expected to disrupt and strain the water supply in the Northeast (Horton et al. 2014), with rising temperatures causing increased evaporative demand, decreased winter snowpack, and earlier snowmelt (Trombulak and Wolfson 2004; Burns et al. 2007; Hayhoe et al. 2007; Xue and Ullrich 2021). Examining the large-scale meteorological conditions associated with dry spells in this region fosters deeper understanding of the meteorological processes driving dryness and can improve the predictability of anomalous meteorological conditions in a changing climate.

The Northeast has experienced intermittent droughts (Seager et al. 2005) including: 1980 (Namias 1982), 1988–90 (Trenberth et al. 1988), and 1998–2004 (Lyon et al. 2005; Seager 2007). The most severe drought over this region in recent decades occurred from 1962 to 1966 (Namias 1966, 1983; Cook and Jacoby 1977). This drought has served as the standard for assessing future water management practices in the Northeast. Consequently, several studies (e.g., Namias 1966; Barlow et al. 2001; Seager et al. 2012) have focused on examining the unique large-scale meteorological conditions associated with this event. Many of the Northeast's water supply systems were constructed almost 70 years ago (Bone and Pollara 2006); since then both the number of consecutive dry days (Hatfield et al. 2014) and population have increased. Significant economic hardships and water supply strains could follow if drought events were to become more frequent, even if the

Denotes content that is immediately available upon publication as open access.

Supplemental information related to this paper is available at the Journals Online website: https://doi.org/10.1175/MWR-D-23-0141.s1.

Corresponding author: Raymond Sukhdeo, rsukhdeo@ucdavis.edu

DOI: 10.1175/MWR-D-23-0141.1

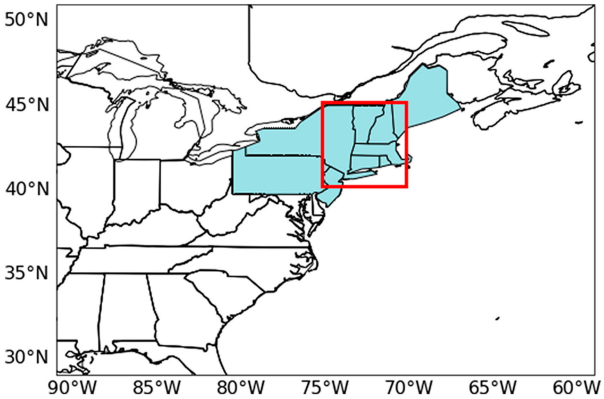

FIG. 1. Geographic domain used in the methodology discussed in section 3. All or parts of the states shaded in blue have some contribution to the region used here. The area enclosed by the red-outlined box is the Northeast as defined for this study. The clustering domain used in section 3 is 30°–50°N, 60°–90°W.

climate is becoming wetter. However, long-term drought events in the Northeast are not associated with a single meteorological driver of persistent below-average precipitation. Instead, these events are often composed of short-term dry periods punctuated by occasional precipitation.

In contrast with longer-duration drought events, short-duration dry spells (events lasting at least a week to several weeks, but shorter than a drought time scale) are more amenable to dynamical analysis because they are dominated by a single meteorological pattern. Model simulations of future climate scenarios suggest that certain watersheds in the Northeast will experience more short-duration dry spells as a result of increased warming and evaporative demand (Hayhoe et al. 2007). Given the current dearth of studies related to understanding the large-scale meteorological conditions associated with short-duration dry spells and the potential risks from an increase in these types of events, the goal of this present work is to fill an important knowledge gap by examining the large-scale meteorological patterns associated with short-duration dry spells over the Northeast.

We focus on short-duration dry spells (i.e., sequential days with daily precipitation below a given threshold) and the meteorological conditions surrounding reduced precipitation in the Northeast. We do not focus on "drought months" because we want to identify and study naturally occurring dry periods of a specified rarity without the artificial constraints of when a month starts or ends. Additionally, our analysis of dry spells is distinguished from that for short-term flash droughts, the latter of which are heavily influenced by increased evaporative stress. For the Northeast, approximately 10% of dry spells last for 12 days or more. For assessing the large-scale meteorological conditions, large-scale meteorological patterns (LSMPs; Grotjahn 2011; Grotjahn et al. 2016) analysis is implemented. LSMP analysis was previously applied to "instantaneous" fields. While time-averaged fields have been linked to LSMPs (Lee and Grotjahn 2019), this is the first study to apply LSMP analysis to time-averaged fields. This is also the first LSMP-based analysis of meteorological conditions associated with persistent dryness, and thus the LSMPs and large-scale meteorological conditions described here may assist dry-spell prediction.

The remainder of the paper is organized as follows. Datasets are described in section 2. Methodology is discussed in section 3. Results and analyses related to the dry-spell LSMPs are provided in section 4. The paper concludes with a summary and discussion in section 5.

2. Data

This study makes use of both daily gauge-based precipitation data and daily reanalysis data. The gauge-based precipitation data come from the CPC Unified Gauge-Based Analysis of Daily Precipitation over the conterminous United States (Xie et al. 2007). These precipitation data have 0.25° × 0.25° grid spacing, with a spatial domain of 20.125°–49.875°N, 230.125°–304.875°E. Reanalysis data are drawn from the ERA5 dataset (Hersbach et al. 2020) with 0.25° × 0.25° grid spacing and the full, global, spatial domain, for the 1961–2021 period. From ERA5, both daily total fields and anomaly fields are considered for selected atmospheric variables. Before calculating daily anomalies for a particular field, the long-term daily mean of that field (1 January–31 December) is calculated and smoothed via Fourier-transform by retaining only the first four harmonics of the yearly cycle. Daily anomalies are then calculated by subtracting that Fourier-transformed long-term daily mean from the total field for individual days. Some of the atmospheric fields we consider include total precipitation, the 500-hPa geopotential height (Z500), 200-hPa zonal wind (U200), 850-hPa specific humidity (Q850), 700-hPa pressure velocity [omega (ω700)], vertically integrated vapor transport (IVT) in the eastward and northward directions, and 925-hPa temperature advection (TA925). The 500-hPa streamfunction field (SF) is calculated via the windspharm Python package (Dawson 2016) using the zonal and meridional winds at 500 hPa.

3. Methodology

a. Event isolation

Space and time criteria are used to identify short-duration dry-spell events from the CPC Unified Gauge precipitation dataset to isolate those events in which most of the region experiences dry conditions at the same time. To begin, the precipitation data are area-averaged in the domain of 40°–45°N, 70°–75°W to generate a daily precipitation time series. This domain omits certain subregions that are in various definitions of "The Northeast" for two reasons. First, parts of a smaller region are more likely to have simultaneous dry conditions than a large region. Second, results for parts of the Northeast outside our region might be estimated by "phase shifting" our LSMPs. Next, we examine consecutive dry days (CDDs). Each "dry day" must have area-averaged precipitation below a threshold. Tested thresholds were: <1, <2, and <3 mm. Others have tested various thresholds; see discussion and additional references in Rivoire et al. (2019). We selected < 2 mm of area-averaged precipitation to define our "dry day" to get both a larger sample size and longer periods of persistent dryness. We use area-

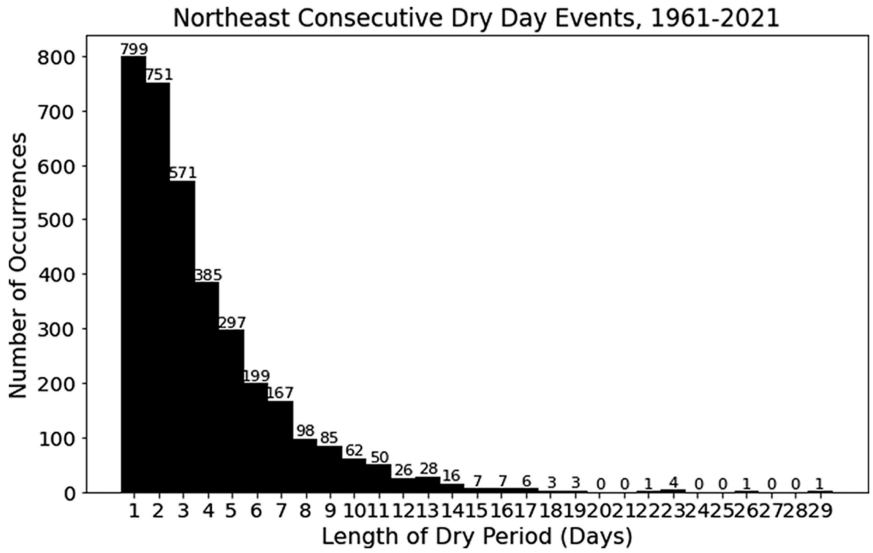

FIG. 2. Histogram distribution of consecutive dry day (CDD) events duration in the Northeast from 1961 to 2021. Lengths of events (days) are given along the x axis, with total number of occurrences given along the y axis. The numbers on top of the histogram bars indicate total count of events for that particular dry-period length. Dry spells in this report are 12 days or longer.

averaged precipitation because we seek a persistent, broader-scale, quasi-stationary, meteorological pattern. Alternatively, low accumulated precipitation, a more appropriate metric for longer-term drought periods, could emerge from intermittent meteorological patterns that may not be amenable to LSMP analysis. The frequency tabulation and duration lengths of these CDD events are shown in the histogram of Fig. 2. The distribution of CDD events approximately follows a geometric distribution fit (GDF) when considering events lasting ≥ 8 days (see the online supplemental material). The GDF assumes no autocorrelation in the data, and when considering events lasting ≥ 1–7 day(s), respectively, autocorrelation in the data leads to the GDF overestimating the probability of these events. Additionally, the GDF to our data implies that there is no preferred CDD duration. Hence, our CDD events of interest are based upon the fraction of all CDDs greater than some threshold duration.

In looking at the right tail end of the distribution, it is seen that the days within events lasting at least 12 days or longer account for roughly 10% of all "dry" days, according to our <2-mm threshold. We thus define "short-duration dry spells" as CDD events in which the number of CDDs is ≥ 12 days. This choice reflects a compromise between obtaining a large enough sample for analysis, while also identifying events that are "extreme" in terms of an extended time with minimal precipitation. This process identifies 103 short-duration dry-spell events. These events range in duration from 12 to 29 days. The start and end dates and duration of the 103 events are given in Table 1. This space and time method identifies short-duration dry spells, but it results in a small sample size of around 1.7 events per year. The reason behind choosing events that are so rare is that the dynamics associated with these dry spells are expected to have a stronger signal that distinguishes them from the "noise" of natural variability.

Two potential issues with the above approach are 1) the atmospheric conditions that reinforce the individual dry-spell events do not "lock in place" at onset but may continue to evolve over time and 2) our 103 events have different total lengths, ranging from 12 to 29 days. To rectify these issues, we utilize a 12-day averaging approach, whereby we time-average the first 12 total days for each event to generate a composite for that individual event. Therefore, we reconstitute our 103 individual dry-spell events as the time-average of the first 12 days (hereinafter, the onset period) of each respective event. This approach addresses the first issue, since the time-average is a filter isolating lower frequency parts of the fields. For the second issue, by using the same time averaging for each respective event, we can now reliably compare the large-scale meteorological conditions associated with the 103 different events.

b. *k-means clustering*

Clustering analysis can group similar patterns among the 103 events, thereby providing a quantitative tool to isolate distinct atmospheric LSMPs associated with the dry spells. In this study, the k-means clustering approach is applied to the 500-hPa SF anomaly fields defined for the 103 dry-spell events in the domain 30°–50°N, 60°–90°W (Fig. 1). This approach is iterative and moves events from one group to another until there is no added improvement in reducing the overall distance between patterns among events in the created groups (Lee and Grotjahn 2016). The distance can be defined as the squared Euclidean point-to-centroid distance in each cluster, where each centroid is the mean of the patterns in its cluster (Späth 1985; Seber 2009). In every iteration step, the clustering process creates clusters objectively. For our analysis, we choose to apply clustering to anomalous 500-hPa SF rather

TABLE 1. Start and end dates and duration (days) of short-duration dry-spell events. Events in italicized font are of mixed type and are excluded from the subsequent analysis in this report.

Event No.	Cluster	Event start date	Event end date	Duration (days)
1	2	3 Jan 1961	15 Jan 1961	13
2	2	16 Oct 1961	29 Oct 1961	14
3	1	14 Mar 1962	30 Mar 1962	17
4	1	15 Apr 1962	28 Apr 1962	14
5	2	27 Jun 1962	8 Jul 1962	12
6	1	5 Apr 1963	17 Apr 1963	13
7	2	5 Oct 1963	27 Oct 1963	23
8	2	24 Apr 1964	8 May 1964	15
9	1	4 Oct 1964	16 Oct 1964	13
10	—	*31 Mar 1965*	*11 Apr 1965*	*12*
11	2	28 Apr 1965	16 May 1965	19
12	—	*20 Jul 1965*	*1 Aug 1965*	*13*
13	1	24 Oct 1965	8 Nov 1965	16
14	1	10 Jan 1966	22 Jan 1966	13
15	1	26 Mar 1966	7 Apr 1966	13
16	1	10 Apr 1966	21 Apr 1966	12
17	—	*21 Oct 1966*	*1 Nov 1966*	*12*
18	2	12 Nov 1966	25 Nov 1966	14
19	2	9 Jan 1967	26 Jan 1967	18
20	—	*27 May 1967*	*7 Jun 1967*	*12*
21	1	4 Feb 1968	29 Feb 1968	26
22	—	*13 Sep 1968*	*24 Sep 1968*	*12*
23	1	4 Mar 1969	19 Mar 1969	16
24	2	7 Oct 1969	19 Oct 1969	13
25	1	1 Jan 1970	17 Jan 1970	17
26	1	4 Apr 1970	19 Apr 1970	16
27	1	21 Mar 1971	2 Apr 1971	13
28	—	*12 Apr 1971*	*24 Apr 1971*	*13*
29	2	22 Sep 1971	5 Oct 1971	14
30	2	12 Oct 1971	23 Oct 1971	12
31	—	*9 Nov 1971*	*21 Nov 1971*	*13*
32	1	5 Jan 1973	19 Jan 1973	15
33	2	7 Oct 1973	19 Oct 1973	13
34	—	*3 Oct 1974*	*14 Oct 1974*	*12*
35	1	18 Oct 1974	30 Oct 1974	13
36	1	7 Apr 1975	18 Apr 1975	12
37	2	15 Jun 1975	28 Jun 1975	14
38	1	3 Apr 1976	15 Apr 1976	13
39	1	7 Nov 1976	28 Nov 1976	22
40	2	21 Oct 1977	3 Nov 1977	14
41	1	9 Feb 1978	3 Mar 1978	23
42	1	22 Apr 1978	4 May 1978	13
43	1	4 Jul 1979	15 Jul 1979	12
44	1	24 Jan 1980	15 Feb 1980	23
45	—	*18 Jan 1981*	*1 Feb 1981*	*15*
46	1	8 May 1981	26 May 1981	19
47	—	*7 Jul 1983*	*19 Jul 1983*	*13*
48	—	*2 Sep 1983*	*16 Sep 1983*	*15*
49	2	5 Oct 1984	21 Oct 1984	17
50	—	*14 Nov 1984*	*28 Nov 1984*	*15*
51	1	14 Mar 1985	31 Mar 1985	18
52	2	12 Sep 1985	23 Sep 1985	12
53	—	*7 Jan 1986*	*18 Jan 1986*	*12*
54	1	23 Feb 1986	6 Mar 1986	12
55	1	11 Feb 1987	22 Feb 1987	12
56	—	*4 Mar 1986*	*20 Mar 1986*	*17*
57	1	21 Feb 1988	3 Mar 1988	12
58	1	11 Mar 1988	24 Mar 1988	14

TABLE 1. (*Continued*)

Event No.	Cluster	Event start date	Event end date	Duration (days)
59	—	*6 Jun 1988*	*19 Jun 1988*	*14*
60	1	30 Nov 1988	13 Dec 1988	14
61	1	18 Apr 1989	29 Apr 1989	12
62	1	17 Dec 1989	29 Dec 1989	13
63	—	*26 Feb 1990*	*11 Mar 1990*	*14*
64	1	18 Jan 1991	30 Jan 1991	13
65	2	19 Oct 1991	30 Oct 1991	12
66	2	16 Jun 1995	1 Jul 1995	16
67	2	16 Aug 1995	31 Aug 1995	16
68	2	12 May 1998	24 May 1998	13
69	2	17 Oct 1998	28 Oct 1998	12
70	1	30 Oct 1998	10 Nov 1998	12
71	—	*14 Apr 2001*	*12 May 2001*	*29*
72	2	7 Nov 2001	19 Nov 2001	13
73	2	4 Aug 2002	16 Aug 2002	13
74	1	10 Jan 2003	2 Feb 2003	23
75	1	7 Sep 2004	18 Sep 2004	12
76	2	8 Feb 2004	21 Feb 2004	14
77	2	23 Feb 2004	5 Mar 2004	12
78	2	9 Apr 2005	20 Apr 2005	12
79	2	2 Sep 2005	14 Sep 2005	13
80	1	16 Mar 2006	1 Apr 2006	17
81	1	20 Jan 2007	2 Feb 2007	14
82	2	13 Apr 2008	28 Apr 2008	16
83	—	*30 Jan 2009*	*11 Feb 2009*	*13*
84	2	13 Mar 2009	26 Mar 2009	14
85	—	*31 Aug 2009*	*11 Sep 2009*	*12*
86	2	2 Nov 2009	13 Nov 2009	12
87	1	5 Jan 2010	17 Jan 2010	13
88	1	27 Jan 2010	10 Feb 2010	15
89	—	*9 Feb 2011*	*24 Feb 2011*	*16*
90	2	29 Jan 2012	16 Feb 2012	19
91	2	15 Nov 2012	27 Nov 2012	13
92	2	25 Apr 2013	8 May 2013	14
93	—	*23 Sep 2013*	*4 Oct 2013*	*12*
94	1	19 Oct 2013	31 Oct 2013	13
95	1	20 Jan 2014	3 Feb 2014	15
96	1	24 Apr 2015	10 May 2015	17
97	—	*27 Aug 2015*	*8 Sep 2015*	*13*
98	1	16 May 2016	29 May 2016	14
99	1	26 Jan 2017	7 Feb 2017	13
100	—	*8 Sep 2017*	*19 Sep 2017*	*12*
101	2	11 Oct 2017	24 Oct 2017	14
102	1	4 Dec 2018	16 Dec 2018	13
103	—	*12 Sep 2020*	*29 Sep 2020*	*18*

than Z500 because SF produces a discernible pattern in the tropics as well as higher latitudes. Additionally, the 500-hPa level is chosen because it is a commonly used level for showing large-scale, upper-level patterns in the midlatitudes.

Two potential concerns arise when applying k-means clustering to atmospheric data: 1) there is some uncertainty in choosing an optimal number of clusters, and 2) assigning an event to one cluster over another is less clear when sample size is small. To address these concerns, first we applied a technique analogous to the "distance of dissimilarity" metric (as in Stefanon et al. 2012) to determine the optimal number k. The number k with a sudden drop of intercluster distance for the next higher value of $k + 1$ is considered the optimal number of clusters. Intercluster distance of our SF anomaly field has a notably abrupt drop from $k = 2$ to higher k. While a larger number of k may lead to less uncertainty in the classification process, the goal of the clustering analysis is to gain physical insight into the conditions surrounding the events without creating a distinct group for each event (Lee and Grotjahn 2016).

The distance of dissimilarity metric, as well as our visual inspection of individual events, led us to choose $k = 2$ clusters in this study. Additionally, spatial projection analysis is applied [as in Lee and Grotjahn (2016)] to assess how well

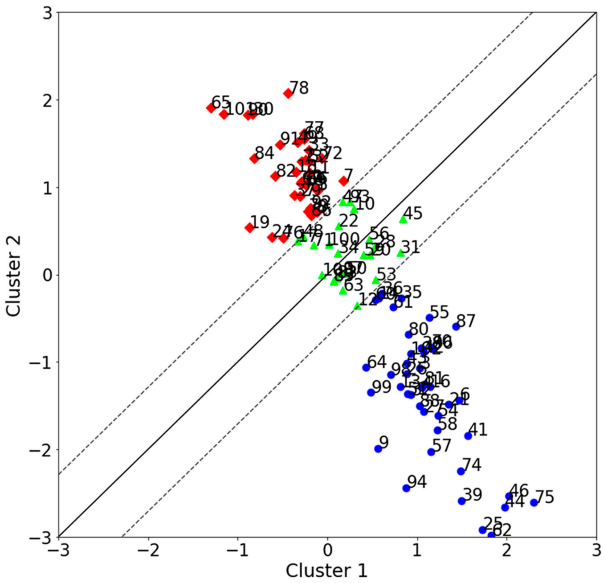

FIG. 3. Scatterplot of two projection coefficients for each of the 103 events. The numbers match the event numbers specified in Table 1. Blue dots mark events in cluster 1, red diamonds mark events in cluster 2, and green triangles mark mixed events and fall within the dashed lines. Dashed lines are used as a visual aid to show the separation of cluster-1 and cluster-2 events from mixed events. The shift of the dashed lines from the 1:1 line is 0.70. For individual events, the anomalous 500-hPa streamfunction field is projected onto the composite means of the two clusters. A total of 34 mixed events are excluded from the analysis hereinafter.

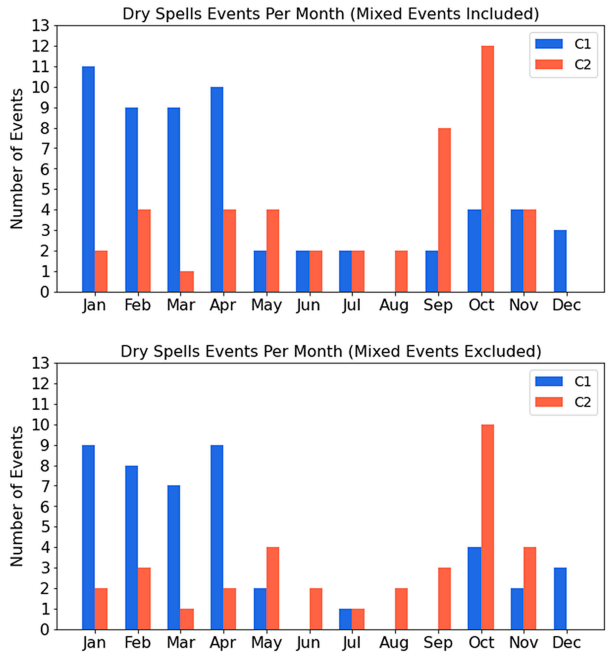

FIG. 4. Distribution of dry-spell events by month: (top) mixed events included, and (bottom) mixed events excluded; C1 denotes cluster 1, and C2 denotes cluster 2.

individual events are sorted into the two clusters. Projection coefficients p_{kj} of the jth event against the kth cluster composite means are calculated for the same domain of the 500-hPa streamfunction anomaly above:

$$p_{kj} = \frac{\sum_{i=1}^{N}(x_i^j y_i^k)}{\sum_{i=1}^{N}(y_i^k)^2}, \quad \text{for } k = 1, 2 \text{ and } j = 1, n,$$

where k is a cluster, j identifies an individual event, n is the total number of events ($n = 103$), i is a specific grid point, N is the total number of grid points, x is the field of a variable of individual events j to be projected, and y^k is the composite mean field of x for cluster k.

The projection coefficients are plotted on a scatterplot in Fig. 3. In the scatterplot, individual events generally fall into groups along a diagonal line between two groups where the projection on one cluster mean is much higher than the projection onto the other cluster mean. The two cluster means will be shown as two ways in which the synoptic pattern creates similar conditions *over our region of interest*. We want to identify as many events as we can that are assignable to one or the other cluster. In Fig. 3, we see that there are some events that project weakly and/or similarly onto both cluster means. These events, here labeled "mixed" (those depicted in-between the dashed lines), will not be considered in detail, and were determined as follows: Initially, the clustering algorithm was applied to all events as detailed above using $k = 2$. Then initial cluster composite means were calculated from the constituents of the respective clusters. Next, each event was projected onto both initial cluster composite means. Final cluster membership requires each event to fall outside of the two dashed lines in Fig. 3. Events falling between the dashed lines were declared to be mixed events and were excluded from the final sets of cluster constituents. The separation of events during the SF clustering process is also relatively insensitive to reasonable changes in the domain boundaries (of ±5°), and similar composite means are generated when a different clustering field is used (i.e., Z500 instead of SF; see the online supplemental material).

Of the 103 events initially identified, 34 mixed events were excluded. Cluster 1 is left with 45 events, and cluster 2 is left with 34 events. Within these clusters, events are further grouped by month to reveal seasonal differences. Monthly distributions are shown in Fig. 4. The winter (DJF) and spring (MAM) periods for cluster 1, along with the fall (SON) period for cluster 2, have the larger sample sizes of events. As such, we focus on these three combinations of cluster type and season in section 4. The LSMPs for these combinations are shown in Fig. 5. Results for other seasons are shown in the online supplemental material.

c. *Wave activity flux*

To track the propagation of wave energy, we use the wave activity flux (WAF), as formulated in Takaya and Nakamura (2001) (hereinafter, TN01), to track the propagation of wave

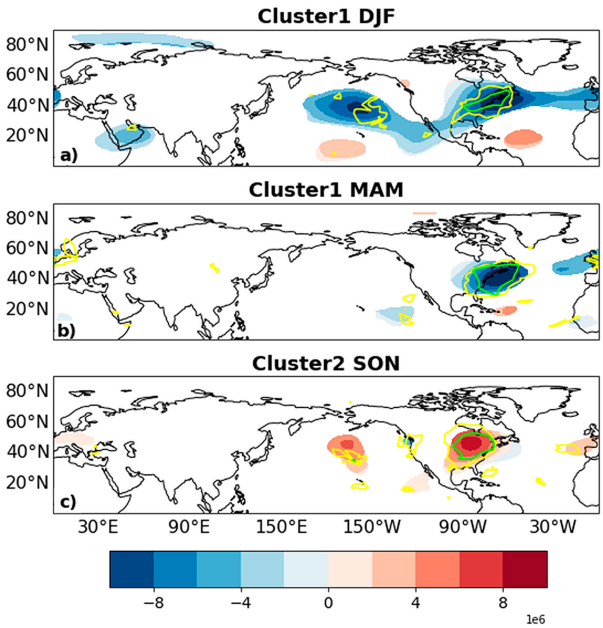

FIG. 5. Large-scale meteorological patterns, defined by the 500-hPa streamfunction anomaly field ($m^2 s^{-1}$; contours), for the short-duration dry-spell events in cluster 1 in (a) DJF (20 events) and (b) MAM (18 events) and in (c) cluster 2 in SON (17 events). Contour shading indicates areas of significance determined by bootstrap resampling. Yellow and green contours indicate the sign count magnitude of 0.6 and 0.8, such that 80% and 90% of the members in the cluster have the same sign, respectively. Streamfunction values are scaled by 10^6.

energy. This method allows one to analyze specific periods in time, like the wave activity flux developed by Plumb (1986). We use the quasi-stationary WAF formulation to track the time evolution of wave activity associated with the development of the dry-spell events. TN01 show that this wave activity is locally parallel to the group velocity of quasigeostrophic Rossby wave packets. Convergence of WAF at a ridge in geopotential is expected to amplify the ridge, while the same ridge would decay if WAF was diverging there. Depending on where the convergence and divergence of WAF occurs relative to the geopotential pattern, these areas can be interpreted as driving both the propagation and amplitude changes of troughs and ridges. The TN01 WAF formulation has been used to study the dynamics of many phenomena, such as blocking formation over Siberia (Nakamura et al. 1997; TN01) and the formation of hot spells in the California Central Valley during the summertime (Lee and Grotjahn 2016). Here, WAF is used to interpret the respective trough and ridge formations in the LSMPs that are associated with short-duration dry spells in the Northeast. Our results focus on analyzing WAF in conjunction with the SF anomaly. Similar results are obtained using the WAF as defined in Plumb (1986) (see the online supplemental material).

d. *Lead–lag composites*

Another tool that is used to understand the time evolution of the dry-spell events is to form composites of total and daily anomaly fields for atmospheric fields for the clusters at fixed times prior to and after the dry spells, for individual events. For the prior time period, we look at 3, 2, and 1 day(s), respectively, before the onset start date for each individual event. For each of these periods, the events are averaged to generate composites. The composites for these days represent our "lead" periods. An analogous procedure constructs the lag periods, in which the "lag" periods are 1, 2, and 3 day(s), respectively, after each *individual* dry-spell events has ended.

The lead and lag periods for the events in cluster-1 DJF, cluster-1 MAM, and cluster-2 SON show differences between the clusters in the development of the corresponding LSMPs and related dynamics. The patterns and their evolution are consistent among the events within a cluster subgrouping. The consistency is measured by using a sign counts procedure (Grotjahn 2011), which involves counting the number of events whose corresponding anomaly field has the same sign of the cluster mean anomaly at each grid point. Sign counts are calculated as follows: in a cluster, the number of events with a negative sign at a grid point is subtracted from the number of events having positive sign at that grid point; that difference is then divided by the total number of events in that cluster. This facilitates comparison among clusters that have a different number of events. For example, a sign count of 1.0 would indicate that all events in that cluster have positive anomaly at a particular grid point. A sign count of −1/3 means that 2/3 of the events have negative anomaly at that grid point. The sign counts procedure is combined with significance from a bootstrap test to identify true LSMPs (Reed et al. 2022). The bootstrap compares the cluster mean with a large number [$O(1000)$] of random means formed from the same membership size and drawn with replacement. Regions where the cluster mean is <5% or ≥95% of the random means are labeled significant for the LSMP composites.

4. Two different types of dry-spell events

a. *Evolution of precipitation anomalies*

The evolution of the precipitation anomalies for the three combinations is considered first. While negative anomalies are located over the Northeast during the onset period for each season, there are some differences in their evolution. For cluster-1 DJF, a negative precipitation anomaly develops in the lower Mississippi Valley region at two days before onset (Fig. 6b) and strengthens until onset (Fig. 6d). This strengthening coincides with the development of negative precipitation anomalies over the Atlantic coast and the Northeast. Similar development is observed with cluster-1 MAM, with the gradual strengthening of the negative anomaly near the Gulf Coast and Northeast (Figs. 6i–l). Cluster-2 SON does exhibit the same strong negative anomaly near the Gulf Coast; but the negative anomalies are more widespread across the central United States (Fig. 6s). The strongest negative anomalies first occur over the Northeast at the onset (Figs. 6d,l,t). The dry anomaly persists for the whole dry spell (Figs. 6e,m,u). In all three combinations, it is apparent that dry anomalies are present across large portions of the eastern United States in the period before and during the dry spells,

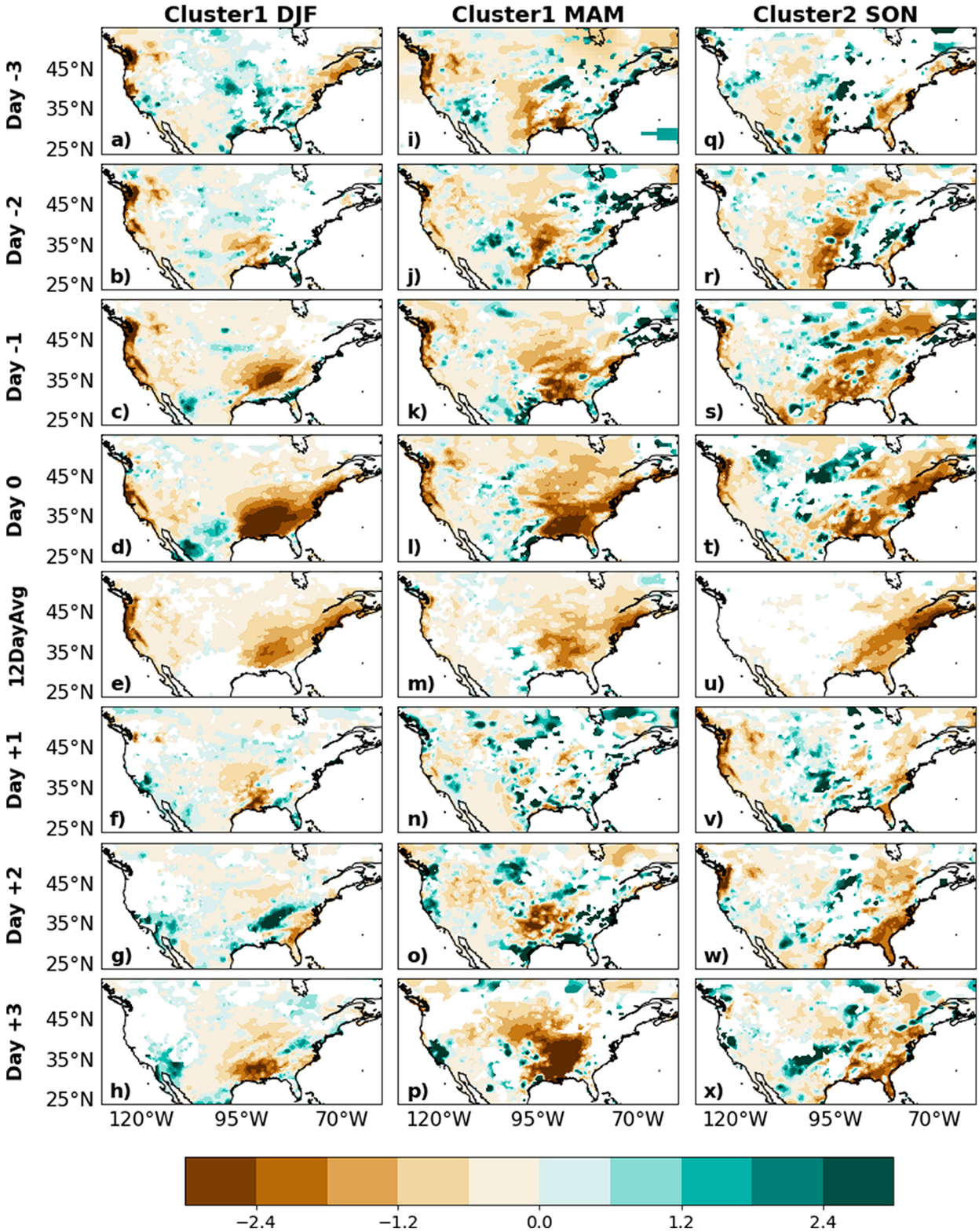

FIG. 6. Evolution of composites of total precipitation anomaly (mm day^{-1}; shading) for the cluster type and season indicated by the label at the top of each column for (a),(i),(q) 3 days before onset; (b),(j),(r) 2 days before onset; (c),(k),(s) 1 day before onset; (d),(l),(t) onset; (e),(m),(u) 12-day dry-spell period; (f),(n),(v) 1 day after dry spells end; (g),(o),(w) 2 days after dry spells end; and (h),(p),(x) 3 days after dry spells end. For the anomaly field, grid points are plotted only when the sign count has magnitude greater than $1/3$ (thus $2/3$ of the members have the same sign).

and are not confined solely to the Northeast. This indicates that Northeast dry spells are typically part of a much larger region of reduced precipitation. Additionally, the expansive dry anomalies along the eastern United States, especially during winter, suggest changes to the trajectory of midlatitude weather systems. Our results will confirm this by finding a narrowing and shifting southward of the frontal cyclone storm track along the Atlantic seaboard during the dry-spell events.

b. *Dynamical differences driving two types of dry spells: SF, WAFs, and jet stream*

We now develop a dynamical picture of the differences in the evolution of the LSMPs of the three seasons as defined by the 500-hPa SF anomaly and the associated WAF fields (Figs. 7 and 8). Corresponding jet stream field changes are shown in Figs. 9 and 10. Cluster-1 DJF (Fig. 7e) and MAM (Fig. 7m) during dry spells are defined by a strong negative pressure anomaly centered off the midlatitude Atlantic seaboard. Another negative center is found in the central Pacific (Figs. 5a and 7e) in cluster 1 during DJF but not during MAM (Figs. 5b and 7m). Cluster-2 SON, in contrast, features a strong positive pressure anomaly center in east-central North America (Figs. 5c and 8e).

The evolutions toward these SF fields differ between the dry-spell combinations. For cluster-1 DJF, a negative low pressure anomaly is located in the northern Pacific Ocean and in the western United States at three days before onset (Fig. 7a). The central Pacific anomaly slowly develops and expands, while the continental anomaly moves eastward (Figs. 7b,c) and expands at the onset date (Fig. 7d), with both anomalies reaching peak magnitude during the onset period (Fig. 7e). The development of the cluster-1 MAM (Figs. 7i–k) is similar to that of DJF, as a negative anomaly develops in the central United States and moves eastward and expands by the onset date (Fig. 7l), with the notable absence of the negative SF anomaly in the central Pacific. Cluster-2 SON features a strong positive pressure anomaly center in east-central North America (Fig. 8e). For cluster-2 SON, a high pressure anomaly is centered near Maine at three days before onset (Fig. 8a) that begins to move offshore a day later (Fig. 8b). At the same time, a small area of high pressure develops in the central United States. This area strengthens and expands (Fig. 8c) and moves eastward by the onset date (Fig. 8d), with the high pressure area reaching peak magnitude during the onset period (Fig. 8e).

After the dry spells, the low pressure anomaly in the midlatitude Atlantic Ocean for cluster-1 DJF (Figs. 7f–h) and MAM (Figs. 7n–p) weakens and moves farther eastward away from the shore. The low pressure in the central Pacific in cluster-1 DJF is still present but is less expansive in its eastward extent (Figs. 7f–h). Similarly, the high pressure area in cluster-2 SON also weakens and shifts eastward (Figs. 8f–h).

Figures 7 and 8 also show cluster mean WAF vectors for evolution of the dry spells. The WAFs differ between the three combinations in ways partly consistent with the above discussion. In cluster-1 DJF, WAF vectors cross north-central North America with convergence in the midlatitude Atlantic Ocean, just offshore of North America, a location consistent with the build-up of the trough during the day −1 lead plot (Fig. 7c). During the onset period (Fig. 7e), WAF converges into the trough, helping to strengthen and maintain it. Elements of the pattern can travel differently and thus be out of phase (and WAF convergence appears weak) before coming into phase at onset and the onset period. In general, WAF for cluster-1 DJF during the onset period indicates convergence in the midlatitude Atlantic Ocean. By the lag periods (Figs. 7f–h), WAF convergence is weaker near the Northeast, coinciding with the weakening of the trough and its shift eastward. This development is similar for cluster-1 MAM (Figs. 7i–p). In cluster-2 SON, the WAF vectors are often weaker than those in cluster 1 and convergence of WAF is less clear in east-central North America as the high pressure ridge builds up (Figs. 8a–d) and reaches peak strength during the onset period (Fig. 8e). Hence, WAF convergence is less useful in explaining the build-up of the high pressure ridge in cluster-2 SON.

Given the different midtropospheric 500-hPa SF LSMPs, one would expect some differences in the midlatitude jet stream as well. Figures 9 and 10 show total zonal wind (contours) and zonal wind anomaly (shading) at 200 hPa, for the three combinations. In cluster-1 DJF and MAM (Fig. 9), the wind anomaly pattern suggests a narrowing of the jet stream. The northern dipole pair of wind anomalies in the midlatitude Atlantic strengthens and expands the midlatitude jet eastward into the central Atlantic Ocean (Figs. 9d,l) while weakening it over eastern Canada. The total zonal component peaks during the onset period (Figs. 9e,m). As a consequence, the jet stream peak value increases from lead to onset at 25°–45°N from the North American east coast out over the Atlantic, and a clear region of deceleration sets up from Hudson's Bay eastward out over the Atlantic. From balancing terms: zonal advection and ageostrophic Coriolis in the zonal momentum equation, this jet stream deceleration region would have northerly ageostrophic motion. Allowing ageostrophic winds to approximate divergent winds, an upper-level pattern of northerlies over the Great Lakes together with southerly ageostrophic wind to the south (Figs. 11a,b), is consistent with subsidence over the Northeast. Hence, ageostrophic northerlies in the deceleration region coupled with ageostrophic southerlies in the acceleration region (Figs. 11a,b) act to generate upper-level convergence (Figs. 11d,e) and sinking beneath (Figs. 11g,h). This sinking might also be understood from the vorticity equation, where the divergence term and planetary vorticity advection terms may approximately balance (Grotjahn and Osman 2007), such that upper-level northerlies imply convergence. However, farther east, where the northerly ageostrophic winds are northerly (Figs. 11a,b), the zonal wind anomaly is still positive, though weakened downstream over the Atlantic (Figs. 9e,m).

For cluster-2 SON (Fig. 10), a different jet stream anomaly pattern is also observed, though the consequence is similar to that of cluster 1. A negative anomaly centered over the southeastern U.S. quadrant, coupled with a positive anomaly over Hudson's Bay (Fig. 11c), creates acceleration over the east coast of the United States. To the north, a positive anomaly peaks near Hudson's Bay, so the winds decelerate over eastern Canada. These anomalies strengthen the

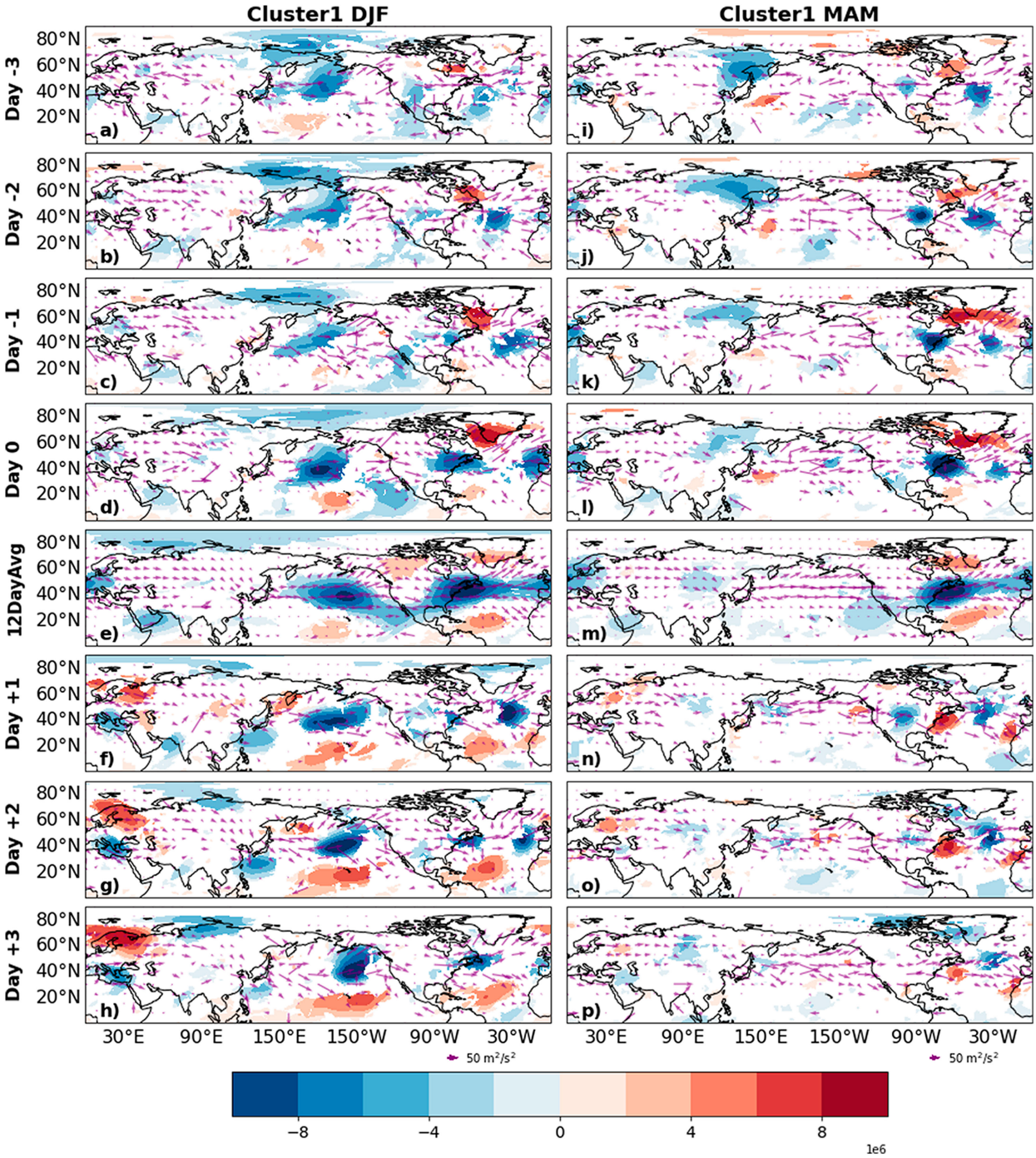

FIG. 7. Similar to Fig. 6, but showing evolution of composites of 500-hPa streamfunction anomaly ($m^2\ s^{-1}$; contours) and total horizontal WAF ($m^2\ s^{-2}$; vectors) for cluster 1 during (a)–(h) DJF and (i)–(p) MAM. For the anomaly field, grid points are plotted only when the sign count has magnitude greater than $1/3$. WAF is plotted only when either the zonal or meridional component has a sign count whose magnitude exceeds $1/3$. Streamfunction is scaled by 10^6.

total zonal component whose value peaks at 2-day lead (Fig. 10b) such that the total wind jet axis is north of the region of interest during the onset period (Fig. 10e). The jet deceleration would imply northerly ageostrophic motion, visible in Fig. 11c. Over northeastern North America, ageostrophic winds turn anticyclonically, creating upper-level convergence (Fig. 11f) and sinking over the Northeast (Fig. 11i).

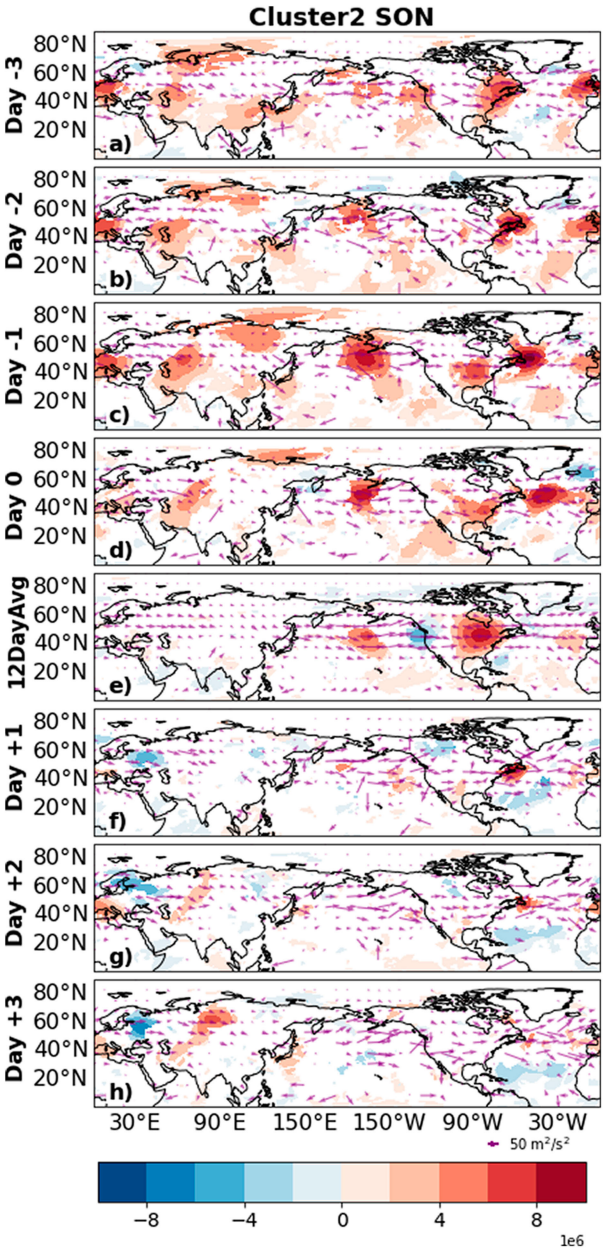

FIG. 8. As in Fig. 7, but showing cluster 2 during SON.

The discussion thus far of the dynamics associated with the dry-spell combinations may be summarized as follows. In cluster 1, WAF accompanies the development of a low pressure area in the midlatitude Atlantic Ocean. Changes to the zonal flow link to ageostrophic motions that foster upper-level convergence and sinking over the Northeast. A high pressure area in east-central North America is built up in cluster-2 SON, with less influence from WAF convergence. While the zonal flow changes also differ from cluster 1, the ageostrophic motions again lead to upper-level convergence and sinking over the Northeast. Next, the thermal and moisture changes critical to the creation of the dry spells are discussed.

c. *Thermodynamical differences driving two types of dry spells*

We now discuss anomalous 700-hPa pressure velocity [omega (ω700)], integrated vapor transport (IVT), 850-hPa specific humidity (Q850), and total 925-hPa temperature advection (TA925), during the onset period of the dry spells, to further the analysis in section 4b. We narrow our discussion to the conterminous United States to focus on local conditions during dry spells.

Upper-level convergence and divergence anticipated from our discussion of the zonal jet stream (U200) anomalies are consistent with ω700 anomalies shown in Fig. 11. In each combination, there are strong, positive ω700 anomalies over the Northeast during the onset period (Figs. 11g–i). Subsidence brings down air having low moisture content over the northeastern United States. Sinking also suppresses cloud formation and precipitation, thereby partly explaining the dry spells.

The horizontal moisture transport (Figs. 11g–i) suggests strong flow off the continent off over our northeastern region in each combination. The IVT vectors circulate in a manner consistent with the SF anomalies shown. Over the Northeast, cluster-1 IVT northerly component occurs on the west side of an anomalous oceanic low, while similar cluster-2 IVT is on the east side of the anomalous continental high. This anomalous flow of moisture into the Northeast likely reduces moisture and also partly explains the dry spells. During the onset period, the counterclockwise (CCW) IVT in cluster 1 is generally strengthened when flowing offshore, but northerly flow into the Northeast is much weaker (Figs. 11g–h). In cluster-2 SON, the clockwise (CW) IVT is strengthened coming up from the Gulf of Mexico, and stronger northerly flow is observed into the Northeast (Fig. 11i) than is observed in cluster 1. Given the importance of southerly IVT along the Atlantic seaboard for providing moisture to this region (Sukhdeo et al. 2022), these results provide additional context for the Q850 anomalies discussed below. As the midlevel streamfunction LSMPs develop, they act to divert the normal IVT away from the Northeast, leading to negative Q850 anomalies there during the onset period. For cluster 1, the IVT anomaly is northeasterly and generally weak as it enters the Northeast during the onset period. In contrast, there is a wrap-around IVT associated with the cluster-2 SON, as the strong high pressure in east-central North America brings moisture-rich air northward into central North America.

The IVT vectors in cluster 1 and cluster 2 are generally similar *locally* over the northeastern region. While they differ away from the region, they are each strong in a different location. One can see how *mixed events can occur when the oceanic low and continental high are both present to suppress clouds and reduce moisture transport.*

For Q850, negative anomalies are located near and over the Northeast during the onset period in the three seasons, with some differences between them. In cluster-1 DJF and MAM, negative Q850 anomalies are centered parallel to the eastern U.S. coast, extending from Louisiana to Maine (Figs. 11g,h). As the midlevel streamfunction LSMPs develop, they act to divert the normal IVT away from the Northeast, leading to negative Q850 anomalies there during the onset period. In cluster-2 SON,

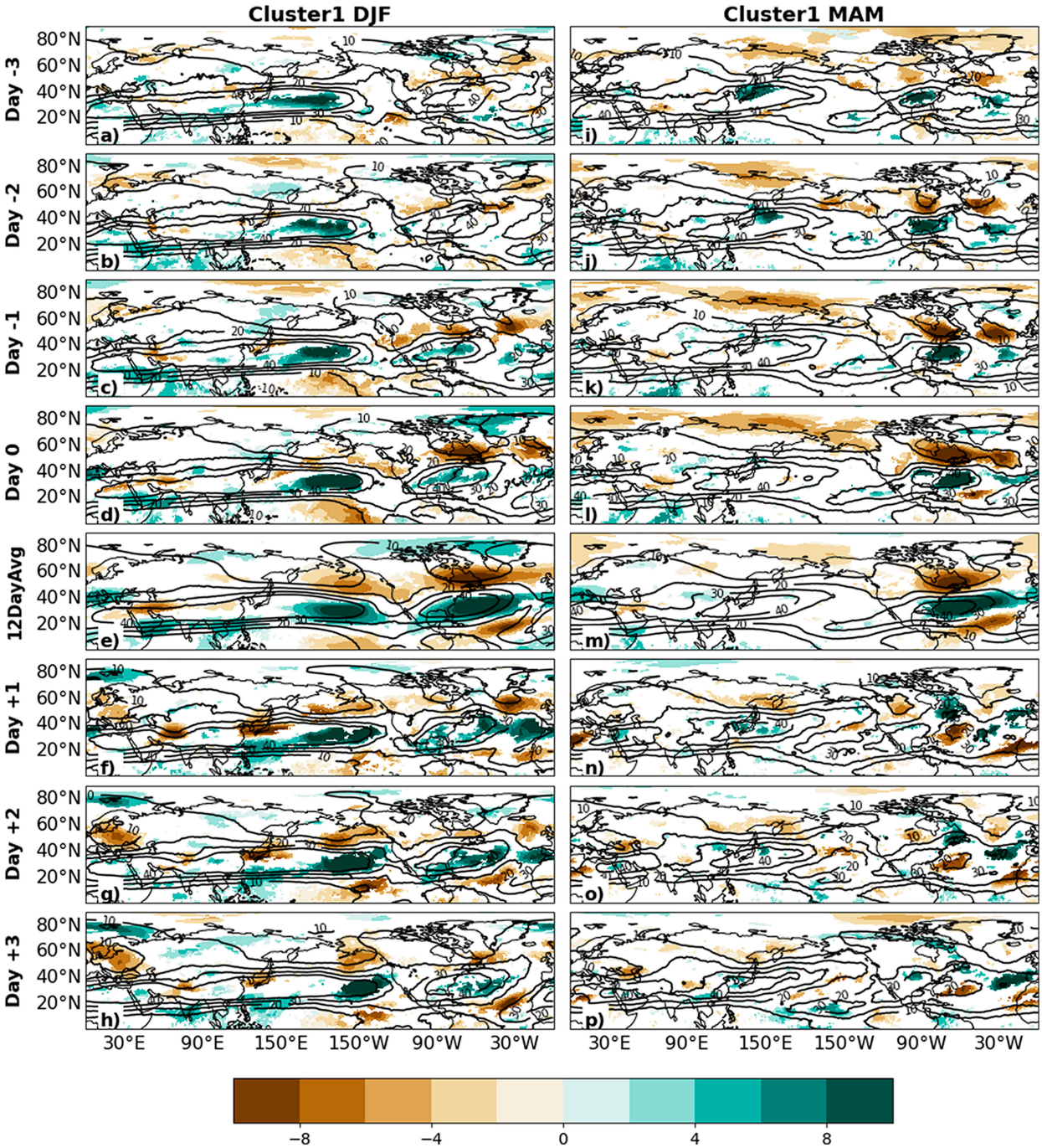

FIG. 9. Similar to Fig. 7, but showing evolution of composites of total zonal wind speed (lined contours) and anomalous zonal winds (shading) at 200 hPa for cluster 1 during (a)–(h) DJF and (i)–(p) MAM. For the anomaly field, grid points are plotted only when the sign count has magnitude greater than 1/3. Contour interval is 2 m s^{-1} for the anomaly field. Only total field contours from 10 to 40 m s^{-1} are plotted, with a 10 m s^{-1} contour interval.

the negative anomalies do not extend as far south and west as in cluster 1, but instead are concentrated over the northeastern United States (Fig. 11i). Strong, positive ω700 anomalies tend to be collocated with these strong, negative Q850 anomalies.

Last, the role of temperature advection is considered, with Figs. 11j–l. showing TA925 for the three combinations. During the onset period for cluster-1 DJF, there is strong cold advection just south of the Northeast in the midlatitude Atlantic Ocean (Fig. 11j). Cluster-1 MAM has

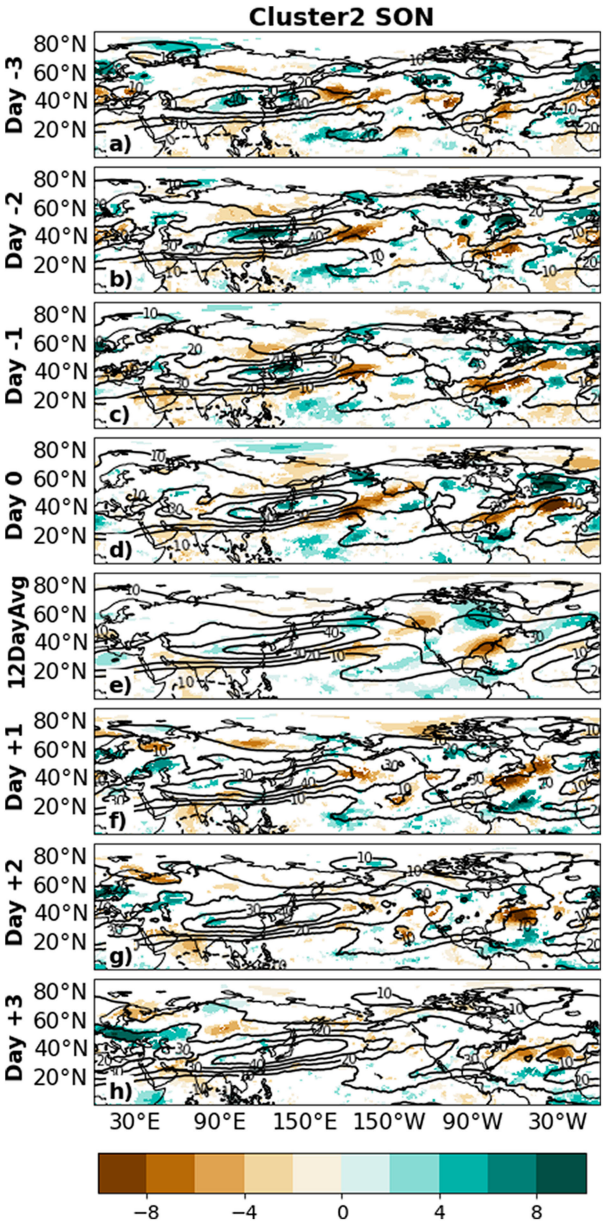

FIG. 10. As in Fig. 9, but showing cluster 2 during SON.

cold advection in the same area, but the magnitude of the advection is much weaker than in DJF (Fig. 11k). The low-level oceanic low off Labrador creates anomalous cold advection to support the anomalous upper-level low to the southwest. For cluster-2 SON (Fig. 11l), there is some cold advection south of the Northeast, and some warm advection just west of the region. The latter supports the anomalous upper-level continental high and is likely due to the CW rotation of the low-level high pressure centered over the southeastern United States. Cold-air advection over the Northeast would reinforce the observed subsidence during the onset period, although the cold-air advection appears to be much weaker for cluster-2 SON.

d. Changes in ETC activity and storm-track density during dry spells

Extratropical cyclones (ETCs) and their tracks play a key role in the seasonal cycle of precipitation in the Northeast (Kunkel et al. 2012; Pfahl and Wernli 2012; Agel et al. 2015; Sukhdeo et al. 2022). There are generally two broad regions with the highest storm track densities: one over the Great Lakes region and another along the Atlantic seaboard (Hoskins and Hodges 2002; Kocin and Uccellini 2004; Pfahl and Wernli 2012; Agel et al. 2015). Track density is typically highest during the winter and spring and is often weaker and shifted more northward into southern Canada during the summer and fall. As we have shown, the short-duration dry spells are in part associated with a suppression of normal onshore IVT, and, given the climatological importance of ETCs for precipitation in the Northeast, it warrants discussing how the dry-spell LSMPs relate to ETC storms tracks. We investigate this by identifying ETC tracks for the time steps in 6-hourly data when ETCs are present in a specific geographic domain relevant to the Northeast. For tracking ETCs, we use the TempestExtremes software package (Ullrich and Zarzycki 2017), which allows for the tracking of pointwise elements within climate datasets. The 6-hourly data for surface pressure (PS) and geopotential at 300 and 500 hPa (Z300 and Z500, respectively) are taken from the ERA5 dataset for the period 1961–2021 and input to TempestExtremes, which then outputs the relevant ETC tracking information, such as time, latitude, and longitude of cyclone centers, and local sea level pressure. Output from TempestExtremes is then selected for geographic relevance to the Northeast (25°–55°N/20°–100°W). From the selected data, we can identify individual ETCs and their associated storm tracks before, during, and after each respective event. Because we are studying events that range in duration from 12 to 29 days, care must be taken when choosing the "after" period for looking at ETC tracks, as longer duration events persist after the 12-day onset period. Since tracks vary seasonally, we identify individual ETCs and their associated storm tracks before, during, and after each respective event. Thus, we define the "before," "during," and "after" periods as follows, using Event 2 (16–29 October 1961) as an example. The during period refers to the first 12 days of a particular dry-spell event (in this case, 16–27 October 1961). For the before period, we use a 12-day lead period (in this case, 4–15 October 1961). Similarly, for the after period, we look at the first 12 days after the end of a particular dry-spell event (in this case, 30 October–10 November 1961).

The track analyses are shown in Fig. 12. During the dry-spell events, ETCs do not pass over the Northeast. This indicates that the dry spells are related to the absence of ETC activity in the region. Additionally, during the dry spells, the ETC storm track is shifted farther south of our region of interest for cluster 1 during DJF and MAM (Figs. 12a–f). During DJF, the southern ETCs are concentrated into a narrower track than other DJF times shown. This concentration supports the anomalous low there in Fig. 5a. This shift is less apparent for cluster-2 SON (Figs. 12g–i). There are also some other key differences before

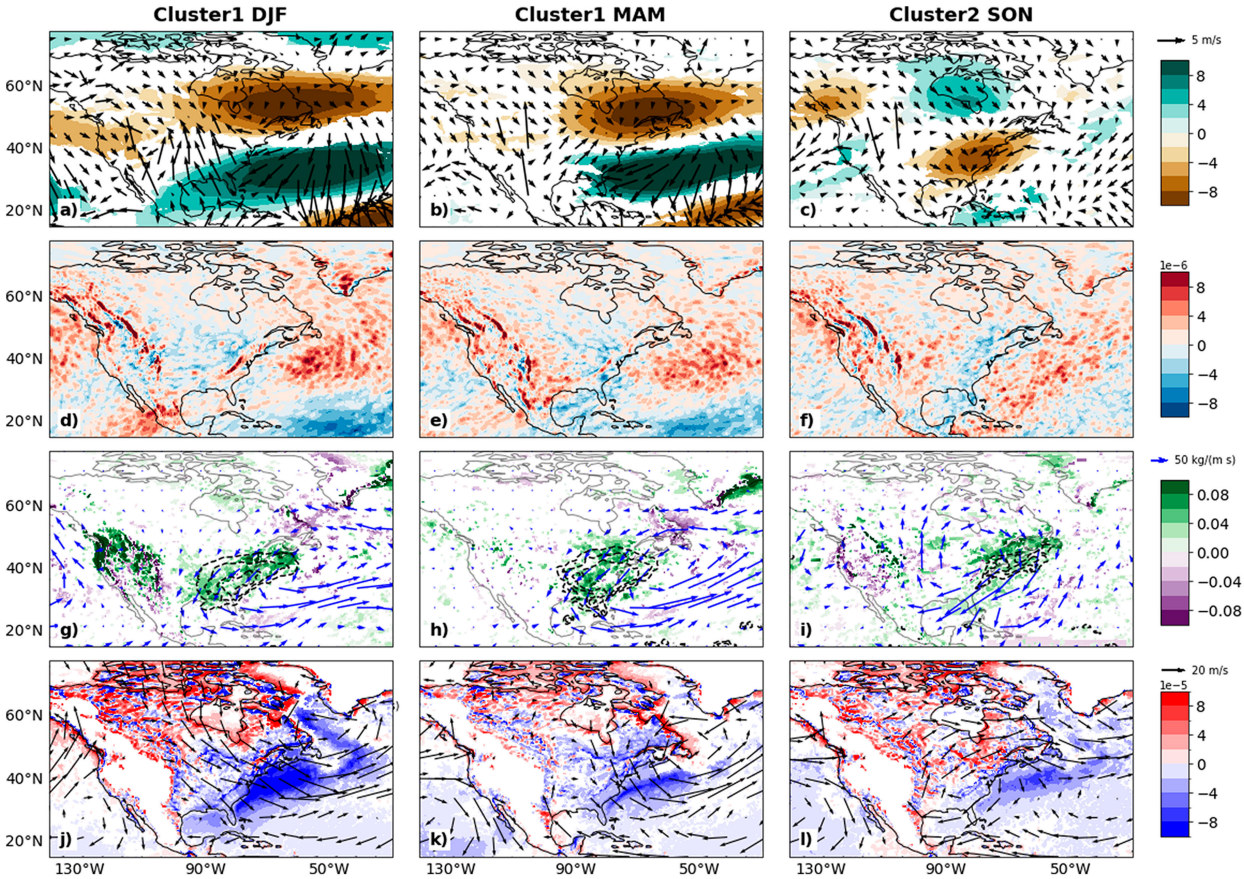

FIG. 11. Several meteorological fields during the 12-day dry-spell period: (a)–(c) Anomalous zonal winds at 200 hPa (m s^{-1}; shading) and total ageostrophic winds at 200 hPa (m s^{-1}; vectors). For the anomaly field, grid points are plotted only when the sign count has magnitude greater than $1/3$. Vectors are plotted only when either the zonal or meridional component has a sign count whose magnitude exceeds $1/3$. (d)–(f) Total horizontal divergence at 200 hPa (s^{-1}; shading). (g)–(i) Anomalous omega at 700 hPa (ω700) (Pa s^{-1}; shading), anomalous specific humidity at 850 hPa (Q850) (g kg^{-1}; contours), and anomalous integrated vapor transport (IVT) [kg (m s)$^{-1}$; vectors]. For all three fields, only grid points with sign count magnitude over $1/3$ are plotted. Vectors are plotted at grid points where either the zonal or meridional component passes the $1/3$ sign counts criterion. Lined contour interval is 0.20 g kg^{-1}, and minimum contour magnitude is 0.55 g kg^{-1}. For clarity, only negative Q850 dashed contours are shown. (j)–(l) Total 925-hPa temperature advection (TA925) (K s^{-1}; shading) and total winds at 925 hPa (m s^{-1}; vectors). For contours, only grid points with sign count magnitude over $1/3$ are plotted. Vectors are plotted at grid points where either the zonal or meridional component passes the $1/3$ sign counts criterion.

and after the dry-spell events. For cluster 1 during DJF and MAM, before and after the dry spells, some of the ETCs moving through the Great Lakes region move southeasterly, and some of the ETCs pass through or nearer to the Northeast. Additionally, the ETC storm track is less concentrated off the Atlantic coast and is more evenly distributed in latitude. For cluster 2 in SON, ETCs are in closer proximity to the Northeast in the before and after periods than they are during the dry spells. These differences between the ETC storm tracks during the dry-spell events versus before and after the dry spells highlight the role that the dry-spell LSMPs have in shifting the storm tracks. These results agree in part with those of Namias (1966), who found that the wintertime circulation near the Northeast during the 1960s drought diverted ETCs away from the region. Overall, our results indicate that the dry-spell LSMPs are consistent with ETC storm tracks being diverted away from the Northeast, with a preference for diversion south of the Northeast during the winter and spring of cluster 1. Sukhdeo et al. (2022) showed that increased ETC density in a similar tracking domain enhances mean precipitation in the Northeast. Here, our results indicate that dry spells occur in part when ETCs do not cross over the region.

e. Seasonality in short-duration dry-spell occurrence

The monthly distribution of short-duration dry-spell events shown in Fig. 4 show seasonal variation in the occurrence of dry spells, with most of the events occurring during the winter, spring, and fall periods. Here, we speculate on why fewer dry-spell events meet our criteria during summer as compared with the other seasons.

Figure 13a shows the monthly averaged time series of large-scale versus convective precipitation from ERA5. Large-scale precipitation is greater than convective precipitation for most of the seasonal cycle, except during the summer. This change in

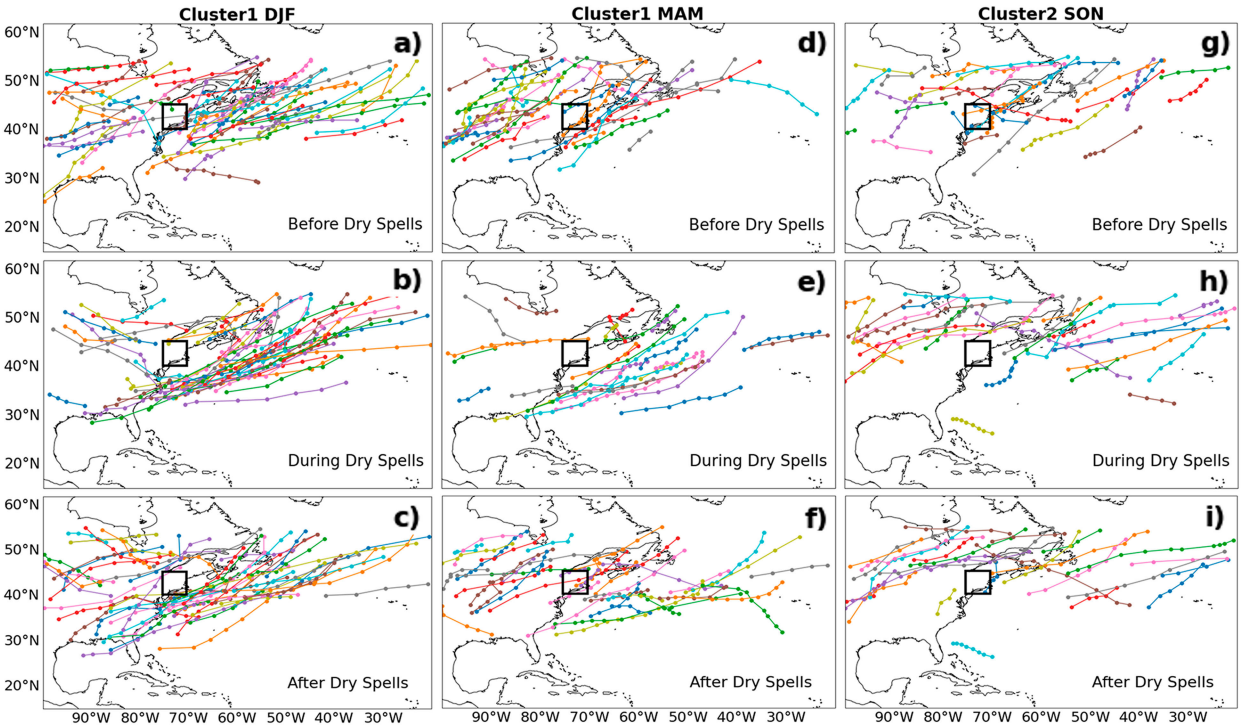

FIG. 12. Extratropical cyclone storm tracks for 12-day periods (a),(d),(g) before; (b),(e),(h) during; and (c),(f),(i) after the dry-spell events. Each line represents an individual ETC storm track. Dots along each ETC storm track represent the location of the cyclone center at 6-h increments during the ETC life span. The black box in each panel is the Northeast region as defined for this study.

precipitation type is primarily related to 1) a reduction in ETC activity in the warm season (see section 4d and the online supplemental material), and 2) an increase in sporadic, localized convection in and around the Northeast (Agel et al. 2015). The decrease in ETC activity can partly be explained by reduced baroclinicity over the warm continent during summer (Gertler and O'Gorman 2019), and by increased localized convection attributed to a warm and moist environment in the Northeast that facilitates greater atmospheric convective instability during the late afternoon and early evening (Hurlbut and Cohen 2014).

The summer period is also unique in terms of its distribution of CDD durations. Figures 13b–e shows CDD histograms for each of the four seasons separately. The winter (DJF), spring (MAM), and fall (SON) periods have mean CDD durations of 4.19, 3.73, and 4.05 days, respectively. For the summer period, the mean CDD duration is nearly a day shorter (3.01 days). The summer period also has a much larger percentage (and number) of events lasting only 1 or 2 days as compared with the other seasons. Summer has ~10% or more CDD periods than the other seasons, but many fewer CDDs last 12 days or longer.

These results are consistent with the changes in precipitation type in the seasonal cycle. During the winter, spring, and fall, as ETC activity is one of the primary drivers of precipitation (Agel et al. 2015; Sukhdeo et al. 2022), precipitation is concentrated along the ETC "storm track." As the storm track changes position due to a block, then the time elapsed between consecutive ETCs affecting our region is lengthened. In contrast, summer precipitation is less guided by large-scale features, and coupled with enhance instability, convection occurs more frequently and sporadically, so CDD periods are shorter in duration.

f. *How do short-duration dry spells compare with drought months?*

The top roughly 10% of CDD periods are 12 days or longer, a shorter time scale than would be used *if* this was a drought study. Because of this, there can be dry spells that meet our event duration criterion during a month with near-normal (or even above normal) precipitation, depending on what happens during the other days of that month. Hence, some of our CDD events can occur in months that are not "drought" months. Additionally, care must be taken when defining a drought, as the occurrence of a dry spell in a particular month can inaccurately attribute drought conditions to a nondrought month. The question is then what fraction of dry events occurs in drought versus nondrought months?

To understand better the connection between short-duration dry spells and drought months, it is necessary to identify longer-term periods of drought that have specifically impacted the Northeast. Gridded, 3-month standardized precipitation index (SPI) values [formulated on the basis of Guttman (1999)] over the Northeast from 1961 to 2021 are employed to identify drought (SPI ≤ -1) months. The 3-month SPI seems more appropriate than a 1-month SPI here, as it provides a more accurate assessment of short- to medium-term moisture conditions. After identifying these months, we then cross-reference the dates of the

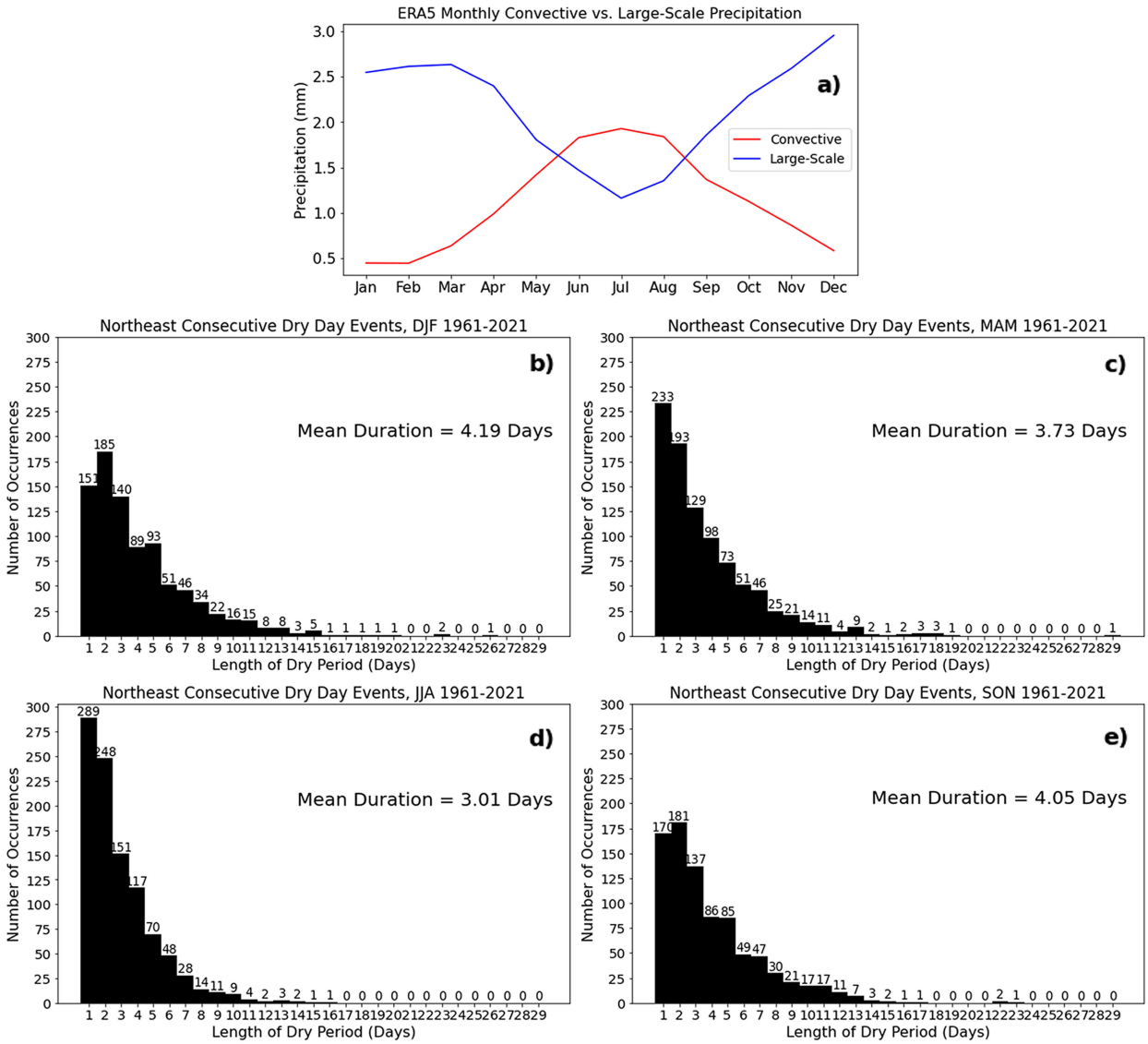

FIG. 13. (a) Time series plot of area-averaged, monthly large-scale vs convective precipitation over the Northeast from ERA5 (1961–2021), and CDD histograms for (b) winter (DJF), (c) spring (MAM), (d) summer (JJA), and (e) fall (SON) from 1961–2021. Histograms use the same format as in Fig. 2. Mean duration in each panel is the average CDD event duration for that season. The total number of dry spells lasting 12 days or longer in each season, including mixed type is 29 for DJF, 30 for MAM, 10 for JJA, and 34 for SON. The total number of dry spells for all CDD events of any duration in each season, including mixed type, is 874 for DJF, 920 for MAM, 1009 for JJA, and 863 for SON.

short-duration dry spells with these drought months to determine the number of our dry-spell events that occur in these months (Readers can find tables listing specific drought months and the dry-spell events in those months in the online supplemental material). During 1961–2021, ~15% (111/732) of the months are so-identified as drought months, while ~27% (28/103) of our dry spells occur during those months, using the 3-month SPI. Alternatively, ~18% (131/732) of the months are so-identified as drought months, and ~44% (45/103) of our dry spells occur during those months, using the 1-month SPI. Since the ratios differ, a 1-month SPI seems inappropriate for assessing a connection between short-duration dry spells and "drought" months, as the occurrence of a dry spell (12 days or longer) in a month can lead to a biased correlation with a low 1-month SPI value for that month. With the stricter drought criteria of the 3-month SPI, only about a quarter ($N = 28$) of dry-spell events are associated with short- to medium-term drought conditions. This indicates that there is only a small connection between dry spells and drought, and while dry spells can occur during longer-term droughts, more dry spells occur during nondrought conditions.

5. Summary and discussion

In this study, LSMPs related to short-duration dry spells in the Northeast are examined. These LSMPs are identified via the use of k-means clustering on the 500-hPa streamfunction

anomaly data for CDD events lasting at least 12 days or longer, and two clusters are shown to adequately represent the data. The key findings from our study are as follows:

1) There is a seasonal preference for DJF and MAM in cluster 1 and for SON in cluster 2.
2) Cluster 1 is associated with a strong anomalous trough stretching from the midlatitude North American east coast across much of the midlatitude Atlantic Ocean. The pressure trough associated with the first cluster has a north-south zonal wind dipole anomaly that shifts the Atlantic midlatitude zonal jet stream to the south; that dipole anomaly enhances upper-level convergence and sinking motion beneath. This sinking motion, coupled with cold-air advection into the Northeast, and accompanied by negative Q850 anomalies due to sinking and changes in horizontal moisture transport, produces an environment of lower-than-normal moisture that suppresses precipitation.
3) Cluster 2 is associated with a strong anomalous ridge over the North American continent that creates a downstream dipole structure in the upper-level zonal wind anomaly that also produces upper-level convergence. Given that cold-air advection is weaker here than in the first cluster, the sinking motion is consistent with upper-level convergence and subsidence from the midlevel high pressure area to the west. This sinking motion, coupled with negative Q850 anomalies due to subsidence and changes to horizontal moisture transport, also suppresses precipitation.
4) Dry spells occur much less frequently during JJA than in other seasons because of the limited influence of ETCs and higher frequency of localized convective precipitation.
5) ETC storm tracks are diverted away from the Northeast during the dry spells, thereby reducing precipitation from ETCs.
6) Individual dry spells can have a mix of the larger-scale features of both cluster means, and so individual events lie on a continuum between two distinct clusters.
7) More dry spells occur in nondrought months than in drought months, meaning that dry spells can occur without preexisting drought conditions.

Our results provide several promising opportunities for further investigation. Several studies have linked large-scale circulation patterns associated with precipitation variability to low-frequency modes of climate variability, such as the North Atlantic Oscillation (NAO) (e.g., Wallace and Gutzler 1981; Barnston and Livezey 1987), the El Niño–Southern Oscillation (ENSO) (e.g., Trenberth 1997), the Pacific–North American pattern (PNA) (e.g., Wallace and Gutzler 1981; Leathers et al. 1991), and the Madden–Julian oscillation (MJO) (reviewed in Zhang 2013). Several studies (Namias 1966; Barlow et al. 2001; Seager 2007; Seager et al. 2012) have shown that these climate modes can influence drought-like conditions over the Northeast. Winter precipitation is more significantly related to the large-scale circulation than in other seasons (Ning et al. 2012a), and as determined in Archambault et al. (2008), Ning and Bradley (2014) and Sukhdeo et al. (2022), these climate modes can have significant influences on certain large-scale patterns that overlap the Northeast region. Any linkage between short-duration dry spells and these low-frequency and remote modes is left for future work.

Historical model simulations can be compared with our reanalysis results to determine the fidelity of models in capturing short-duration dry-spell properties: the cluster mean structures and their frequency, duration, and intensity. In turn, end-of-century model simulations by those models can be utilized to gain insight into how these dry-spell events may change in future periods. Such work would provide important insight regarding future precipitation conditions in the Northeast.

Acknowledgments. This research was supported by the Regional and Global Model Analysis (RGMA) program area(s) in the U.S. Department of Energy's Office of Biological and Environmental Research as part of the multiprogram, collaborative Integrated Coastal Modeling (ICoM) project. Author Paul A. Ullrich was supported by Department of Energy Office of Science Award DE-SC0016605, "A Framework for Improving Analysis and Modeling of Earth System and Intersectoral Dynamics at Regional Scales (HyperFACETS)." Ullrich and author Richard Grotjahn have been supported by the National Institute of Food and Agriculture, U.S. Department of Agriculture, hatch project under California Agricultural Experiment Station Project Accessions 1016611 and 1010971, respectively. The authors certify that they have no affiliations with or involvement in any organization or entity with any financial interest, or nonfinancial interest, in the subject matter or materials discussed in this paper.

Data availability statement. CPC Unified Gauge precipitation data are freely available online (https://psl.noaa.gov/data/gridded/data.unified.daily.conus.html) as cited in Xie et al. (2007). Preprocessed data from the ERA5 dataset are freely available online (https://cds.climate.copernicus.eu/#!/search?text=ERA5&type=dataset) as cited in Hersbach et al. (2020). Some of the postprocessed ERA5 data that were analyzed for this work are available from ZENODO (https://dx.doi.org/10.5281/zenodo.8043725). Other postprocessed data are available from the authors upon reasonable request. The standardized precipitation indices used in this study are available online (https://www.ncei.noaa.gov/pub/data/nidis/indices/nclimgrid-monthly/). Data analysis for this study was conducted using the Anaconda software distribution of the Python programming language and its included packages and modules. Anaconda is available online (https://anaconda.com/). The 500-hPa SF field was calculated using the windspharm Python package as cited in Dawson (2016). Documentation and instructions for installation of windspharm can be found online (https://ajdawson.github.io/windspharm/latest/). The scripts used to calculate WAF (https://github.com/laishenggx/T-N_Wave-Activity-Flux) and Plumb flux (https://github.com/kuchaale/3D_Plumb_flux) are available online. ETC tracking was done using the TempestExtremes software package as cited in Ullrich and Zarzycki (2017). Documentation and instructions for installation of TempestExtremes can be found online (https://github.com/ClimateGlobalChange/tempestextremes). Maps created as part

of this study were generated using the Cartopy Python package and its associated dependencies. Documentation and instructions for installation of Cartopy are online (https://scitools.org.uk/cartopy/docs/latest/).

REFERENCES

Agel, L., M. Barlow, J.-H. Qian, F. Colby, E. Douglas, and T. Eichler, 2015: Climatology of daily precipitation and extreme precipitation events in the Northeast United States. *J. Hydrometeor.*, **16**, 2537–2557, https://doi.org/10.1175/JHM-D-14-0147.1.

Archambault, H. M., L. F. Bosart, D. Keyser, and A. R. Aiyyer, 2008: Influence of large-scale flow regimes on cool-season precipitation in the northeastern United States. *Mon. Wea. Rev.*, **136**, 2945–2963, https://doi.org/10.1175/2007MWR2308.1.

Barlow, M., S. Nigam, and E. H. Berbery, 2001: ENSO, Pacific decadal variability, and U.S. summertime precipitation, drought, and streamflow. *J. Climate*, **14**, 2105–2128, https://doi.org/10.1175/1520-0442(2001)014<2105:EPDVAU>2.0.CO;2.

Barnston, A. G., and R. E. Livezey, 1987: Classification, seasonality, and persistence of low-frequency atmospheric circulation patterns. *Mon. Wea. Rev.*, **115**, 1083–1126, https://doi.org/10.1175/1520-0493(1987)115<1083:CSAPOL>2.0.CO;2.

Bone, K., and G. Pollara, Eds., 2006: *Water-Works: The Architecture and Engineering of the New York City Water Supply*. Monacelli Press, 268 pp.

Burns, D. A., J. Klaus, and M. R. McHale, 2007: Recent climate trends and implications for water resources in the Catskill Mountain region, New York, USA. *J. Hydrol.*, **336**, 155–170, https://doi.org/10.1016/j.jhydrol.2006.12.019.

Cook, E. R., and G. C. Jacoby Jr., 1977: Tree-ring-drought relationships in the Hudson Valley, New York. *Science*, **198**, 399–401, https://doi.org/10.1126/science.198.4315.399.

Dawson, A., 2016: Windspharm: A high-level library for global wind field computations using spherical harmonics. *J. Open Res. Software*, **4**, e31, https://doi.org/10.5334/jors.129.

Gertler, C. G., and P. A. O'Gorman, 2019: Changing available energy for extratropical cyclones and associated convection in Northern Hemisphere summer. *Proc. Natl. Acad. Sci. USA*, **116**, 4105–4110, https://doi.org/10.1073/pnas.1812312116.

Grotjahn, R., 2011: Identifying extreme hottest days from large scale upper air data: A pilot scheme to find California Central Valley summertime maximum surface temperatures. *Climate Dyn.*, **37**, 587–604, https://doi.org/10.1007/s00382-011-0999-z.

——, and M. Osman, 2007: Remote weather associated with North Pacific subtropical sea level high properties. *Int. J. Climatol.*, **27**, 587–602, https://doi.org/10.1002/joc.1423.

——, and Coauthors, 2016: North American extreme temperature events and related large scale meteorological patterns: A review of statistical methods, dynamics, modeling, and trends. *Climate Dyn.*, **46**, 1151–1184, https://doi.org/10.1007/s00382-015-2638-6.

Guttman, N. B., 1999: Accepting the standardized precipitation index: A calculation algorithm. *J. Amer. Water Resour. Assoc.*, **35**, 311–322, https://doi.org/10.1111/j.1752-1688.1999.tb03592.x.

Hatfield, J., G. Takle, R. Grotjahn, P. Holden, R. C. Izaurralde, T. Mader, E. Marshall, and D. Liverman, 2014: Agriculture. *Climate Change Impacts in the United States: The Third National Climate Assessment*, J. M. Melillo, Terese (T. C.) Richmond, and G. W. Yohe, Eds., U.S. Global Change Research Program, 150–174, https://doi.org/10.7930/J02Z13FR.

Hayhoe, K., and Coauthors, 2007: Past and future changes in climate and hydrological indicators in the U.S. northeast. *Climate Dyn.*, **28**, 381–407, https://doi.org/10.1007/s00382-006-0187-8.

Hersbach, H., and Coauthors, 2020: The ERA5 global reanalysis. *Quart. J. Roy. Meteor. Soc.*, **146**, 1999–2049, https://doi.org/10.1002/qj.3803.

Horton, R., and Coauthors, 2014: Northeast. *Climate Change Impacts in the United States: The Third National Climate Assessment*, J. M. Melillo, Terese (T. C.) Richmond, and G. W. Yohe, Eds., U.S. Global Change Research Program, 371–395.

Hoskins, B. J., and K. I. Hodges, 2002: New perspectives on the Northern Hemisphere winter storm tracks. *J. Atmos. Sci.*, **59**, 1041–1061, https://doi.org/10.1175/1520-0469(2002)059<1041:NPOTNH>2.0.CO;2.

Hurlbut, M. M., and A. E. Cohen, 2014: Environments of northeast U.S. severe thunderstorm events from 1999 to 2009. *Wea. Forecasting*, **29**, 3–22, https://doi.org/10.1175/WAF-D-12-00042.1.

Kocin, P. J., and L. W. Uccellini, 2004: *Northeast Snowstorms*. Vols. 1 and 2, *Meteor. Monogr.*, No. 54, Amer. Meteor. Soc., 818 pp., https://doi.org/10.1007/978-1-878220-32-5.

Kunkel, K. E., D. R. Easterling, D. A. R. Kristovich, B. Gleason, L. Stoecker, and R. Smith, 2012: Meteorological causes of the secular variations in observed extreme precipitation events for the conterminous United States. *J. Hydrometeor.*, **13**, 1131–1141, https://doi.org/10.1175/JHM-D-11-0108.1.

Leathers, D. J., B. Yarnal, and M. A. Palecki, 1991: The Pacific/North American teleconnection pattern and United States climate. Part I: Regional temperature and precipitation associations. *J. Climate*, **4**, 517–528, https://doi.org/10.1175/1520-0442(1991)004<0517:TPATPA>2.0.CO;2.

Lee, Y.-Y., and R. Grotjahn, 2016: California Central Valley summer heat waves form two ways. *J. Climate*, **29**, 1201–1217, https://doi.org/10.1175/JCLI-D-15-0270.1.

——, and ——, 2019: Evidence of specific MJO phase occurrence with summertime California Central Valley extreme hot weather. *Adv. Atmos. Sci.*, **36**, 589–602, https://doi.org/10.1007/s00376-019-8167-1.

Lyon, B., N. Christie-Blick, and Y. Gluzberg, 2005: Water shortages, development, and drought in Rockland County, New York. *J. Amer. Water Resour. Assoc.*, **41**, 1457–1469, https://doi.org/10.1111/j.1752-1688.2005.tb03812.x.

Melillo, J. M., T. C. Richmond, and G. W. Yohe, 2014: *Climate Change Impacts in the United States: The Third National Climate Assessment*. U.S. Global Change Research Program, 841 pp., https://doi.org/10.7930/J0Z31WJ2.

Nakamura, H., M. Nakamura, and J. L. Anderson, 1997: The role of high- and low-frequency dynamics in blocking formation. *Mon. Wea. Rev.*, **125**, 2074–2093, https://doi.org/10.1175/1520-0493(1997)125<2074:TROHAL>2.0.CO;2.

Namias, J., 1966: Nature and possible causes of the northeastern United States drought during 1962–65. *Mon. Wea. Rev.*, **94**, 543–554, https://doi.org/10.1175/1520-0493(1966)094<0543:NAPCOT>2.3.CO;2.

——, 1982: Anatomy of Great Plains protracted heat waves (especially the 1980 U.S. summer drought). *Mon. Wea. Rev.*, **110**, 824–838, https://doi.org/10.1175/1520-0493(1982)110<0824:AOGPPH>2.0.CO;2.

——, 1983: Some causes of United States drought. *J. Climate Appl. Meteor.*, **22**, 30–39, https://doi.org/10.1175/1520-0450(1983)022<0030:SCOUSD>2.0.CO;2.

Ning, L., and R. S. Bradley, 2014: Winter precipitation variability and corresponding teleconnections over northeastern United

States. *J. Geophys. Res. Atmos.*, **119**, 7931–7945, https://doi.org/10.1002/2014JD021591.

——, M. E. Mann, R. Crane, and T. Wagener, 2012a: Probabilistic projections of climate change for the mid-Atlantic region of the United States: Validation of precipitation downscaling during the historical era. *J. Climate*, **25**, 509–526, https://doi.org/10.1175/2011JCLI4091.1.

Pfahl, S., and H. Wernli, 2012: Quantifying the relevance of cyclones for precipitation extremes. *J. Climate*, **25**, 6770–6780, https://doi.org/10.1175/JCLI-D-11-00705.1.

Plumb, R. A., 1986: Three-dimensional propagation of transient quasi-geostrophic eddies and its relationship with the eddy forcing of the time–mean flow. *J. Atmos. Sci.*, **43**, 1657–1678, https://doi.org/10.1175/1520-0469(1986)043<1657:TDPOTQ>2.0.CO;2.

Reed, K. A., and Coauthors, 2022: Metrics as tools for bridging climate science and applications. *Wiley Interdiscip. Rev.: Climate Change*, **13**, e799, https://doi.org/10.1002/wcc.799.

Rivoire, P., Y. Tramblay, L. Neppel, E. Hertig, and S. M. Vicente-Serrano, 2019: Impact of the dry-day definition on Mediterranean extreme dry-spell analysis. *Nat. Hazards Earth Syst. Sci.*, **19**, 1629–1638, https://doi.org/10.5194/nhess-19-1629-2019.

Seager, R., 2007: The turn of the century North American drought: Global context, dynamics, and past analogs. *J. Climate*, **20**, 5527–5552, https://doi.org/10.1175/2007JCLI1529.1.

——, Y. Kushnir, C. Herweijer, N. Naik, and J. Velez, 2005: Modeling of tropical forcing of persistent droughts and pluvials over western North America: 1856–2000. *J. Climate*, **18**, 4065–4091, https://doi.org/10.1175/JCLI3522.1.

——, N. Pederson, Y. Kushnir, J. Nakamura, and S. Jurburg, 2012: The 1960s drought and the subsequent shift to a wetter climate in the Catskill Mountains region of the New York City watershed. *J. Climate*, **25**, 6721–6742, https://doi.org/10.1175/JCLI-D-11-00518.1.

Seber, G. A. F., 2009: *Multivariate Observations*. Wiley Series in Probability and Statistics, Vol. 252, John Wiley and Sons, 686 pp.

Späth, H., 1985: *Cluster Dissection and Analysis: Theory, FORTRAN Programs, Examples*. Prentice-Hall, 226 pp.

Stefanon, M., F. D'Andrea, and P. Drobinski, 2012: Heatwave classification over Europe and the Mediterranean region. *Environ. Res. Lett.*, **7**, 014023, https://doi.org/10.1088/1748-9326/7/1/014023.

Sukhdeo, R., P. A. Ullrich, and R. Grotjahn, 2022: Assessing the large-scale drivers of precipitation in the northeastern United States via linear orthogonal decomposition. *Climate Dyn.*, **59**, 3657–3681, https://doi.org/10.1007/s00382-022-06289-y.

Takaya, K., and H. Nakamura, 2001: A formulation of a phase-independent wave-activity flux for stationary and migratory quasigeostrophic eddies on a zonally varying basic flow. *J. Atmos. Sci.*, **58**, 608–627, https://doi.org/10.1175/1520-0469(2001)058<0608:AFOAPI>2.0.CO;2.

Trenberth, K. E., 1997: The definition of El Niño. *Bull. Amer. Meteor. Soc.*, **78**, 2771–2777, https://doi.org/10.1175/1520-0477(1997)078<2771:TDOENO>2.0.CO;2.

——, G. W. Branstator, and P. A. Arkin, 1988: Origins of the 1988 North American drought. *Science*, **242**, 1640–1645, https://doi.org/10.1126/science.242.4886.1640.

Trombulak, S. C., and R. Wolfson, 2004: Twentieth-century climate change in New England and New York, USA. *Geophys. Res. Lett.*, **31**, L19202, https://doi.org/10.1029/2004GL020574.

Ullrich, P. A., and C. M. Zarzycki, 2017: TempestExtremes: A framework for scale-insensitive pointwise feature tracking on unstructured grids. *Geosci. Model Dev.*, **10**, 1069–1090, https://doi.org/10.5194/gmd-10-1069-2017.

Wallace, J. M., and D. S. Gutzler, 1981: Teleconnections in the geopotential height field during the Northern Hemisphere winter. *Mon. Wea. Rev.*, **109**, 784–812, https://doi.org/10.1175/1520-0493(1981)109<0784:TITGHF>2.0.CO;2.

Walsh, J., and Coauthors, 2014: Our changing climate. *Climate Change Impacts in the United States: The Third National Climate Assessment*, J. M. Melillo, Terese (T. C.) Richmond, and G. W. Yohe, Eds., U.S. Global Change Research Program, 19–67, https://doi.org/10.7930/J0KW5CXT.

Xie, P., A. Yatagai, M. Chen, T. Hayasaka, Y. Fukushima, C. Liu, and S. Yang, 2007: A gauge-based analysis of daily precipitation over East Asia. *J. Hydrometeor.*, **8**, 607–626, https://doi.org/10.1175/JHM583.1.

Xue, Z., and P. Ullrich, 2021: A retrospective and prospective examination of the 1960s U.S. northeast drought. *Earth's Future*, **9**, e2020EF001930, https://doi.org/10.1029/2020EF001930.

Zhang, C., 2013: Madden–Julian oscillation: Bridging weather and climate. *Bull. Amer. Meteor. Soc.*, **94**, 1849–1870, https://doi.org/10.1175/BAMS-D-12-00026.1.